Available online at www.sciencedirect.com
SCIENCE DIRECT®
ELSEVIER
International Journal of Solids and Structures 43 (2006) 784–806
INTERNATIONAL JOURNAL OF SOLIDS and STRUCTURES
www.elsevier.com/locate/ijsolstr

Three-dimensional numerical simulation of Vickers indentation tests

J.M. Antunes [a], L.F. Menezes [b], J.V. Fernandes [b,*]

[a] *Escola Superior de Tecnologia de Abrantes, Instituto Politécnico de Tomar, Rua 17 de Agosto de 1808, 2200 Abrantes, Portugal*
[b] *CEMUC, Departamento de Engenharia Mecânica, Faculdade de Ciências e Tecnologia, Polo 2 da Universidade de Coimbra, Pinhal de Marrocos, P-3030-201 Coimbra, Portugal*

Received 11 October 2004; received in revised form 24 February 2005
Available online 12 April 2005

Abstract

The development of depth sensing indentation equipment has allowed easy and reliable determination of two of the most popular measured mechanical properties of materials: the hardness and the Young's modulus. However, some difficulties emerge in the experimental procedure to calculate accurate values of these properties. This is related to, for example, the tip geometrical imperfections of the diamond pyramidal indenter and the definition of the contact area at the maximum load. Being so, numerical simulation of ultramicrohardness tests can be a helpful tool for better understanding of the influence of these parameters on procedures for determining the hardness and the Young's modulus. For this purpose, specific finite element simulation software, HAFILM, was developed to simulate the ultramicrohardness tests. Different mesh refinements were tested because of the dependence between the values of the mechanical properties and the size of the finite element mesh. Another parameter studied in this work is the value of the friction coefficient between the indenter and the sample in the numerical simulation. In order to obtain numerical results close to reality, a common geometry and size of the imperfection of the tip of Vickers indenter was taken into account for the numerical description of the indenter.

Keywords: Numerical simulation; Vickers indentation

* Corresponding author. Tel.: +351 239 790700; fax: +351 239 790701.
E-mail address: jorge.antunes@dem.uc.pt (J.V. Fernandes).

0020-7683/$ - see front matter © 2005 Elsevier Ltd. All rights reserved.
doi:10.1016/j.ijsolstr.2005.02.048

1. Introduction

The ultramicrohardness test is commonly used to measure the materials mechanical properties. The most obvious of these properties is the hardness, which can be defined by the equation:

$$H = \frac{P}{A}, \tag{1}$$

where P is the maximum applied load and A is the contact area of the indentation immediately before unloading.

The experimental determination of the contact area, A, can be a hard task, when using ultramicrohardness test. In fact, the high performance attained by the current depth sensing indentation equipment in load and displacement resolutions allows for the use of ultra-low loads. However, the use of indirect methods is needed as well as the consideration of specific aspects for the contact area evaluation (see, e.g., Trindade et al., 1994; Antunes et al., 2002a; Oliver and Pharr, 1992), which are not common in the case of the classic microhardness tests, for which the size of the indentation is measured by optical means. The main aspects to be considered are related to the geometrical imperfections of the tip of the diamond pyramidal punch and the formation of pile-up or the presence of sink-in, which influence the shape and size of the indentation.

The ability of the ultramicrohardness equipment to register the load versus the depth indentation, during the test, enables us to evaluate not only the hardness, but also other properties, such as the Young's modulus. Based on the Sneddon relationship (Sneddon, 1965) between the indentation parameters and Young's modulus, Doerner and Nix (1986) have proposed an equation that relates the Young's modulus with the compliance of the unloading curve immediately before unloading, C, and the contact area, A, such as:

$$E_{\mathrm{R}} = \frac{\sqrt{\pi}}{2}\frac{1}{\sqrt{A}}\frac{1}{C}, \tag{2}$$

In this equation, E_{R}, is the reduced Young's modulus, which is a function of the Young's modulus and the Poisson's ratio, v, of the specimen (s) and the indenter (i), through:

$$\frac{1}{E_{\mathrm{R}}} = \frac{1-v_{\mathrm{s}}^2}{E_{\mathrm{s}}} + \frac{1-v_{\mathrm{i}}^2}{E_{\mathrm{i}}}. \tag{3}$$

Such as for the hardness calculation, the evaluation of the Young's modulus needs the correct determination of the contact area. Moreover, the correct determination of the compliance is needed for the evaluation of the Young's modulus.

The use of the numerical simulation to study the deformation process involved in the indentation test seems to be a useful tool for understanding the mechanical phenomena that takes place into the material under indentation. In the last few years, many works have used the numerical simulation to describe the indentation process. However, most of them use bi-dimensional analyses with spherical and conical indenters, and sometimes a load distribution is used instead of the indenter (see, e.g., Murakami and Yuang, 1992; Laursen and Simo, 1992; Sun et al., 1995; Cai and Bangert, 1995; Kral et al., 1993; Bolshakov et al., 1996; Taljat et al., 1998; Bhattacharya and Nix, 1988, 1991). Some works (see, e.g., Zeng et al., 1995; Wang and Bangert, 1993; Antunes et al., 2002b), show results from three-dimensional numerical simulations of the hardness tests with Vickers indenter, but in general do not take into account the friction, between the indenter and the indented material, and the existence of the offset in the tip of the indenter.

In the present study specific simulation software, HAFILM was developed to simulate ultramicrohardness tests. This home code enables us to simulate hardness tests with any type of indenter shape including the offset imperfection of the indenter tip and takes into account the friction between the indenter and the sample. A preliminary analysis on the influence of the finite element mesh refinements and on the friction coefficient on the hardness and Young's modulus numerical calculations is performed. In the following, a

detailed numerical study about the size influence of the offset of the indenter on those mechanical properties is presented, using indenters with five different offset values. Finally, the influence of the work hardening on the indentation geometry and its consequences on the contact area, hardness and Young's modulus evaluation, is studied.

2. Mechanical model

The mechanical model, which is the base of the FEM home code HAFILM, considers the ultramicrohardness test as a process of large plastic deformations and rotations. The plastic behaviour of the material can be described by the anisotropic Hill's yield criterion with isotropic and/or kinematic work hardening (in the present study the material is assumed as isotropic—Von Mises criterion—and described by an isotropic work hardening law). The elastic behaviour is isotropic. It is assumed that contact with friction exists between the sample and the rigid indenter. To model the contact problem, a classical Coulomb law is used. To associate the static equilibrium problem with the contact with friction an augmented Lagrangean method is applied in the mechanical formulation. This leads to a mixed formulation, where the kinematic (material displacements) and static variables (contact forces) are the final unknowns of the problem. For its resolution, the HAFILM code uses a fully implicit algorithm of Newton–Raphson type. All non-linearities, induced by the elastoplastic behaviour of the material and by the contact with friction, are treated in a single iterative loop (Menezes and Teodosiu, 2000).

2.1. Elastoplastic formulation

The elastoplastic constitutive equation can be written as (Oliveira et al., 2003):

$$\dot{\boldsymbol{\sigma}}^J = \boldsymbol{C}^{\mathrm{ep}} : \boldsymbol{D}, \tag{4}$$

where $\boldsymbol{C}^{\mathrm{ep}}$ is a fourth order tensor designed as elasto-plastic modulus, $\boldsymbol{D}$ is the strain rate tensor and $\dot{\boldsymbol{\sigma}}^J$ is the Jaumann derivative of the Cauchy stress tensor $\boldsymbol{\sigma}$:

$$\dot{\boldsymbol{\sigma}}^J = \dot{\boldsymbol{\sigma}} + \boldsymbol{\sigma}\boldsymbol{W} - \boldsymbol{W}\boldsymbol{\sigma}, \tag{5}$$

where $\dot{\boldsymbol{\sigma}}$ is the temporal derivate of the Cauchy stress tensor and $\boldsymbol{W}$ is the rotation rate tensor defined by:

$$\boldsymbol{W} = \dot{\boldsymbol{R}}\boldsymbol{R}^{\mathrm{T}}, \tag{6}$$

$\boldsymbol{R}$ being the elastic rotation tensor.

The plastic behaviour is described by using the general yield condition:

$$f(\bar{\sigma}, Y) = \bar{\sigma} - Y = 0. \tag{7}$$

In this equation Y is the flow stress in tension, which is a function of a scalar parameter that represents the isotropic work-hardening, as described by the Swift law:

$$Y = C(\varepsilon_0 + \bar{\varepsilon}^{\mathrm{p}})^n, \tag{8}$$

where C, ε_0 and n are constants for a particular material, determined in classical mechanical tests and $\bar{\varepsilon}^{\mathrm{p}}$ is the equivalent plastic strain. The yield stress of the material Y_0, is given by the equation:

$$Y_0 = Y(\bar{\varepsilon}^{\mathrm{p}} = 0) = C\varepsilon_0^n. \tag{9}$$

In Eq. (7), the equivalent stress $\bar{\sigma}$ is defined by the quadratic form:

$$\bar{\sigma}^2 = \boldsymbol{\sigma} : \boldsymbol{M} : \boldsymbol{\sigma}, \tag{10}$$

where $\boldsymbol{M}$ is a fourth order tensor. Their evolution along the deformation process is given as function of the initial anisotropy tensor $\widehat{\boldsymbol{M}}$, corresponding to the Hill criterion:

$$M_{ijkm} = R_{in}R_{jp}R_{kq}R_{ms}\widehat{M}_{npqs}. \tag{11}$$

2.2. Principle of virtual velocities

Let Ω_0 denote the region occupied by the material at a current time t. It is assumed that the contact boundary Σ_0 of Ω_0 can be divided into two parts: $\Sigma_{0|1}$, where the rate of the nominal stress vector is prescribed, and $\Sigma_{0|2}$, on which the velocity vector is prescribed. Then, the principle of virtual velocities equivalent to the incremental boundary-value problem, formed by the equilibrium equations, boundary conditions and constitutive equation (4), goes as follows (Menezes and Teodosiu, 2000):

$$\int_{\Omega_0} \prod : \delta\dot{\boldsymbol{E}}\, \mathrm{d}\Omega = \int_{\Sigma_{0|1}} \boldsymbol{s}^* \delta\boldsymbol{v}\, \mathrm{d}\Sigma. \tag{12}$$

This Eq. (12) is fulfilled for any virtual velocity field δv (with $\delta v = 0$ on $\Sigma_{0/2}$). $\prod$ is the first Piola–Kirchoff stress tensor, with respect to the configuration at time t, and $\boldsymbol{s}$ is a place and time known function.

2.3. Contact with friction

One of the most common difficulties on the numerical simulation of the indentation process is related to the time dependence of the boundary conditions due to the contact with friction between the indenter and the deformable body. To solve this problem, an augmented Lagrangian approach is used to define an equivalent problem that includes in its formulation the restrictions associated with the contact with friction (Menezes and Teodosiu, 2000; Desaxce and Feng, 1991; Simo and Laursen, 1992). The formulated problem leads to the following mixed non-linear system:

$$\begin{cases} [\boldsymbol{F}^{\mathrm{int}}(\boldsymbol{u})] + [\boldsymbol{F}^{\mathrm{equi}}(\boldsymbol{u},\boldsymbol{\lambda})] - [\boldsymbol{F}^{\mathrm{ext}}] \\ [\boldsymbol{F}^{\mathrm{sup}}(\boldsymbol{u},\boldsymbol{\lambda})] \end{cases} = \boldsymbol{R}(\boldsymbol{u},\boldsymbol{\lambda}) = 0, \tag{13}$$

$\boldsymbol{F}^{\mathrm{int}}(\boldsymbol{u})$ and $\boldsymbol{F}^{\mathrm{ext}}$ represent the internal e external forces, $\boldsymbol{F}^{\mathrm{equi}}(\boldsymbol{u},\boldsymbol{\lambda})$ and $\boldsymbol{F}^{\mathrm{sup}}(\boldsymbol{u},\boldsymbol{\lambda})$ are two operators associated to the contact with friction boundary conditions. Eq. (13) presents a system of six equations to six unknown variables, three displacements ($\boldsymbol{u}$) and three contact forces ($\boldsymbol{\lambda}$) (Oliveira et al., 2003).

3. Numerical simulation

3.1. Implicit algorithm

The finite element code HAFILM uses a fully implicit algorithm of Newton–Raphson type to solve the non-linear system. All non-linearities, induced by the elastoplastic behaviour of the material and by the contact with friction, are treated in a single iterative loop (Menezes and Teodosiu, 2000).

The evolution of the deformation process is described by an updated Lagrangian scheme, i.e., the configuration of the deformed body at time t, and is taken as a reference for the time interval $[t,t+\Delta t]$, Δt being the time increment. When the solution for the current time increment is known, the configuration and the state variables are updated and the result is taken as the reference configuration during the subsequent time increment.

3.2. Finite elements

The library of the FEM code HAFILM has three different types of isoparametric solid finite elements: tetrahedron with four nodes, pentahedron with six nodes and hexahedron with eight nodes. The implementation of these elements is very easy, but it needs some cares when applied to problems with large plastic deformations. When the numerical method uses a full integration scheme, the condition of constant volume during plastic deformation, assumed in the mechanical model, leads to an artificial stiffness increase of the elements, that affects the final solution. The use of a selective reduced integration enables to obtain a behaviour improvement of the elements when large deformations are assumed. In the present study, the hydrostatic components of the gradient and virtual velocity are considered constants within the element and are evaluated for its central point (reduced integration point). The other remaining components are evaluated with a full integration scheme.

The spatial discretization of the deformed body leads to a global linear system resulting from the linearization of Eq. (13). This system is calculated and solved in each iteration of the implicit Newton–Raphson algorithm (Menezes and Teodosiu, 2000):

$$\begin{cases} [K_{AB}]_{ij}\{\mathrm{d}u_B\}_j + [T_A]_{ij} + [Q_A]_{ij}\{\mathrm{d}\lambda_A\}_j = \{f_A^1\}_i \\ [T_A]_{ij}\{\mathrm{d}u_A\}_j + [P_A]_{ij}\{\mathrm{d}\lambda_A\}_j = \{f_A^2\} \end{cases} \tag{14}$$

In this system, A and B are the global numbers of the nodes; du and dλ are the nodal vectors of displacement and contact force increments, respectively; $[K_{AB}]_{ij}$ is the global stiffness matrix. The remaining terms of Eq. (14) are directly related to the contact with friction conditions of each node. This system is not symmetric and usually it is ill conditioned, requiring robust methods for its resolution (Alves and Menezes, 2002).

4. Modulation of the indentation process

4.1. Indenter description

The Vickers indenters used in ultramicrohardness tests does not have a perfect geometry. Among the geometric defects, the most important is the so-called ''offset''. The importance of this defect is related to errors introduced in the experimental area evaluation. Bézier surfaces describe the indenter geometry used in the numerical simulations, which allow obtaining a fine description of the tip, as shown in Fig. 1. A detailed view of one fourth of the indenter tip, presenting a rectangular shape is also shown in this figure, where the dimension, a, of the geometrical defect of the tip is indicated (Table 1).

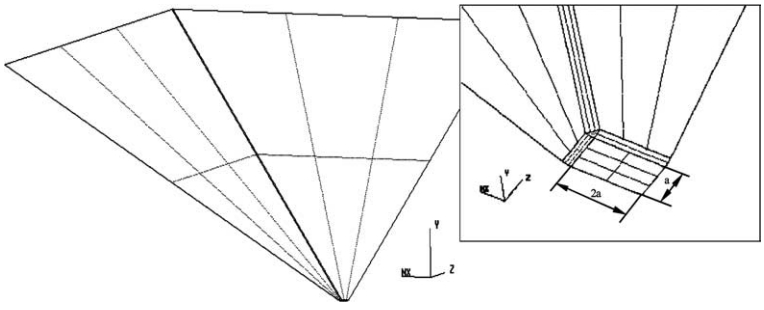

Fig. 1. Vickers indenter and a detail of one fourth the indenter tip with the imperfection designed offset.

Table 1
Indenters offsets

Indenter	Vickers 1	Vickers 2	Vickers 3	Vickers 4	Vickers 5
a (μm)	0.02	0.04	0.06	0.08	0.10

In order to accomplish the study of the aspects related to the indenter geometry, we perform numerical simulations using two different flat indenters: one circular and other with a square geometry, both with three different contact areas (7.1, 21.2 and 40.7 μm^2).

4.2. Sample and materials description

A study concerning the influence of the mesh in the hardness results was performed, using three different meshes, of three-linear eight-node isoparametric hexahedrons. Table 2 presents the size of the elements in the indentation region and the total number of elements that compose each mesh. The mesh refinement was chosen in order to guarantee a good estimation of the indentation contact area. Due to the symmetry along the X- and Z-axis, only a fourth of the sample is used in the simulation as illustrated in Fig. 2. Four real materials were studied, by simulation. Their mechanical properties are presented in Table 3. Also, in the

Table 2
Finite element meshes

Mesh	Mesh 1	Mesh 2	Mesh 3
Element size (μm)	0.380	0.055	0.045
Number of elements	4680	5832	8008

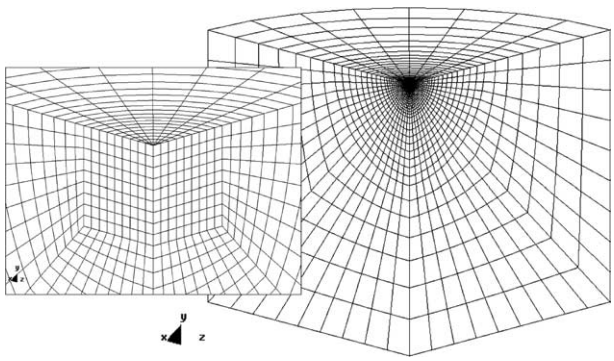

Fig. 2. Finite element mesh used in the numerical simulations.

Table 3
Mechanical properties of the real materials

Material	Y_0 (GPa)	n	E (GPa)	v
Steel AISI M2	4.0	0.010	220	0.290
BK7	3.5	0.010	82	0.203
Tungsten	2.0	0.010	410	0.289
Nickel	0.2	0.078	220	0.310

Table 4
Mechanical properties of the fictitious materials

Materials	Studied cases	n	Y_0 (GPa)		E (GPa)	ε_0	ν
			Minimum	Maximum			
Without work-hardening	10	≈0	0.25	25	100	0.005	0.29
	10		0.50	60	410		
With work-hardening	6	0.6	0.05	6	100		
	6		0.15	6	410		

study, several fictitious materials with two different work-hardening coefficients ($n = 0$ and $n = 0.6$) and two Young's modulus ($E = 100$ GPa and $E = 410$ GPa) were used (Table 4).

5. Experimental and results

5.1. Numerical parameters: mesh and friction coefficient analysis

In order to evaluate the influence of the mesh size in the calculation of the mechanical properties, six numerical simulations with a maximum load $P_{max} = 20$ mN and the two indenters (Vickers 1 and 3) were performed using three different meshes. The material used in this analysis was the steel AISI M2 and the friction coefficient was equal to 0.16.

Fig. 3 presents the hardness results obtained with the three meshes (the hardness value marked in the figure, 10.2 GPa, was obtained by experimental tests, at a maximum load equal to 50 mN, carry out with an ultramicrohardness equipment Fischerscope H100; the indentation contact depth was determined from the unloading curve (Oliver and Pharr, 1992), and the indenter shape function for the tip was obtained using the atomic force microscopy (AFM) technique, as explain in previous work (Antunes et al., 2002a)). The numerical values were determined from the projected contact area on the surface plan of the sample, at the peak load; this area corresponds to the interior of the contour defined by the nodes that contact with the indenter at the maximum load. For Vickers 3, the hardness values are almost independent on the mesh size. However, for Vickers 1, the result for mesh 1 is lower than for mesh 2 or 3, for which the

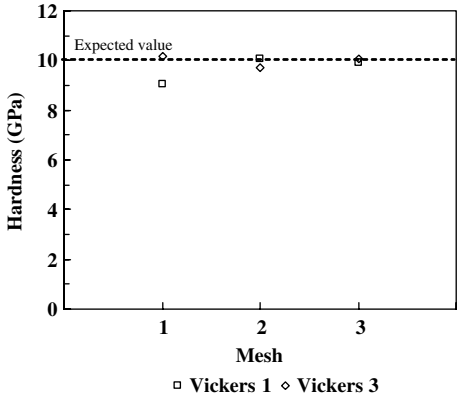

Fig. 3. AISI M2 hardness results obtained with the three studied meshes, for the cases of the indenters Vickers 1 and 3.

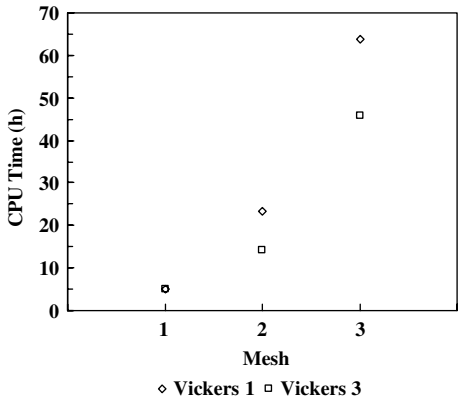

Fig. 4. CPU calculation time spent in the numerical simulations with the three meshes.

results are quite satisfactory. Fig. 4 presents the CPU time used on the simulations, for the same six cases. From Figs. 3 and 4, we can conclude that mesh 2 presents a good compromise between hardness results accuracy and CPU time.

The influence of friction coefficient between the indenter and the deformable body in the hardness results was studied using mesh 2 and indenter Vickers 3. The materials used were the nickel and the steel AISI M2 that were loaded up to 10 and 20 mN respectively. These two materials have different mechanical behaviours: soft and hard material, respectively. In this analysis, the following friction coefficients were tested: 0.04 (only for AISI M2 steel), 0.08, 0.16 and 0.24. The choice of these values is related with the fact that in the literature is common to consider a friction coefficient between the indenter (diamond) and most materials equal to 0.16 (Lynch, 1980; Bowden and Tabor, 1950). The evolution of the calculated hardness with the value of the friction coefficient is presented in Fig. 5. The low variation of the hardness values observed in this figure indicates that the overall behaviour is apparently independent of the value of the friction coefficient used in the simulations. However, as show in Fig. 6(a) and (b) for the AISI M2 steel, the distribution of the equivalent plastic strain under the indenter is quite dependent on the value of the friction coefficient. For low values of the friction coefficient, the maximum value of the equivalent plastic strain is quite high ($\approx$1.27), and it is located on a small area at the surface of the indentation (Fig. 6(a)). In the case of a high

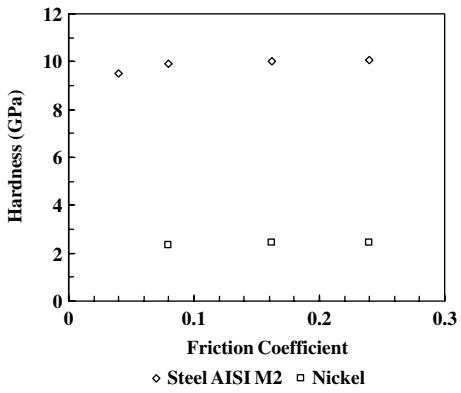

Fig. 5. Hardness results obtained for the different friction coefficients, using mesh 2 and Vickers 3.

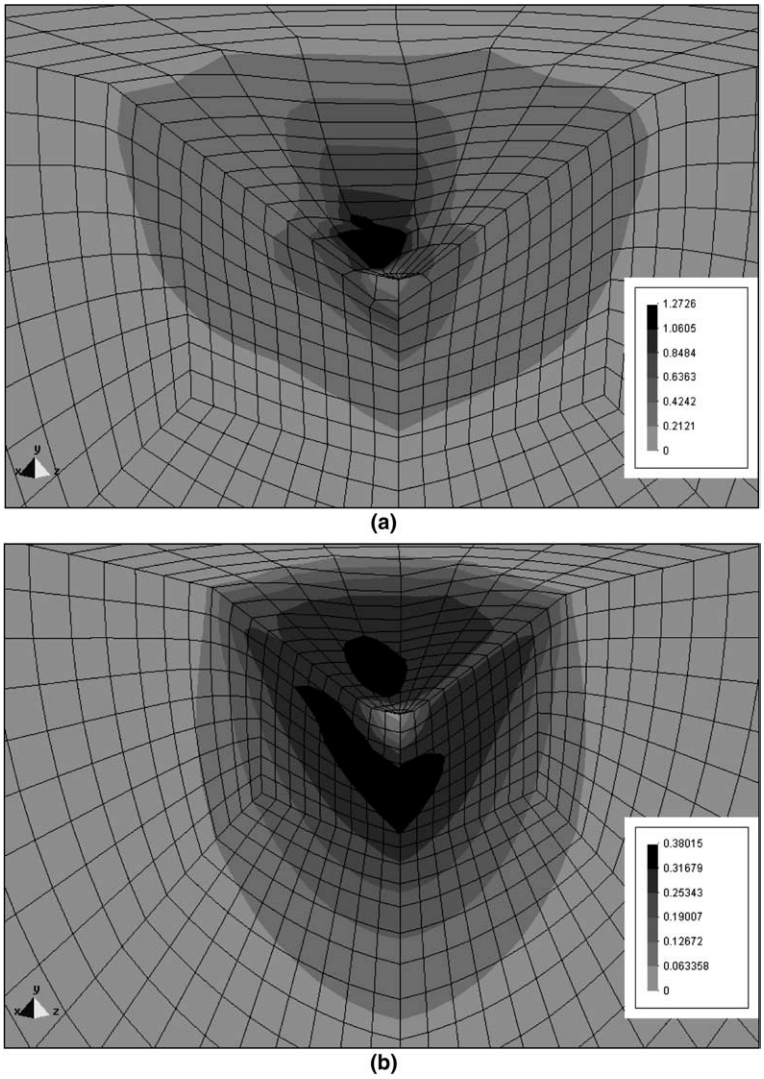

Fig. 6. Equivalent plastic strain distribution on the steel AISI M2 sample: (a) for a friction coefficient equal to 0.04; (b) for a friction coefficient equal to 0.24.

friction coefficient (Fig. 6(b)), the maximum value of the equivalent plastic strain (≈0.38) is lower and it is located not only at the surface but also at a certain depth value under the indentation surface. Moreover, the deepness of the plastic deformed region increases with the value of the friction coefficient. This behaviour, which is also observed for nickel, indicates that with increasing the friction coefficient the strain gradient becomes smooth.

In spite these different behaviours, the hardness values seems to be only slightly influenced by the friction coefficient, at least for the values of the friction coefficient that are commonly used in the literature (Fig. 5). In the following, the value retained for the friction coefficient was 0.16, which is the most common used.

5.2. Compliance evaluation

As mentioned above, it is possible to determine the Young's modulus using the hardness test. To do so, it is necessary to have the previous compliance evaluation, $C = \mathrm{d}h/\mathrm{d}P$ calculated at the point of maximum load, (Eq. (2)). Several experimental methods have been described, using the unloading curve of the hardness test, to estimate C (Doerner and Nix, 1986; Oliver and Pharr, 1992). The stiffness, $S = 1/C = \mathrm{d}P/\mathrm{d}h$, at maximum load during unloading, can be determined by two different ways. One of them takes at about 1/3 of the unloading data (starting from maximum load) and uses a linear fitting (Doerner and Nix, 1986):

$$P = Sh + b, \tag{15}$$

where the stiffness, S, is defined as the initial unloading slope and $b = -Sh_p$, at $P = 0$, where h_p is the interception of the linear unloading curve with the h axis. This method (linear fit) is strongly influenced by the unloading curve fraction considered (see Oliver and Pharr, 1992). A second method, proposed by Oliver and Pharr (1992), suggest the fitting of the unloading curve using the power law:

$$P = A(h - h_\mathrm{f})^m, \tag{16}$$

where h_f is the final depth after unloading, m and A are constants directly obtained from the fit.

In the present work, a fit of the unloading curve with a power law is used, but slightly different from the method of Oliver and Pharr (1992). The term h_f in Eq. (16) is changed in the new equation by h_0, which is the lower value of h used in the fitted region (the unloading curve was fitted by using the commercial software Curve Expert 1.3.), corresponding to a load value P_0. So, Eq. (16) can be rewritten as:

$$P = P_0 + A(h - h_0)^m. \tag{17}$$

A plot of stiffness *versus* fitted fraction of unloading curve, obtained by fitting Eqs. (16) and (17) to the numerical results, is shown in Fig. 7. This figure shows that the results for both equations (16) and (17) are very close, whatever the materials except for the case of the nickel and tungsten. It is also clear from Fig. 7 that the results of stiffness obtained using Eq. (17) are lower and present stabilization (horizontal dashed lines) when the fraction of the upper part of the unloading curve taken into account in the fit is between 60% and 90%. Table 5 presents the Young's modulus results obtained in numerical simulations and experimental tests, for the four studied real materials (Table 3). The numerical Young's modulus results, using the compliance values obtained from Eq. (17), are close to the input values. In fact, the correlation

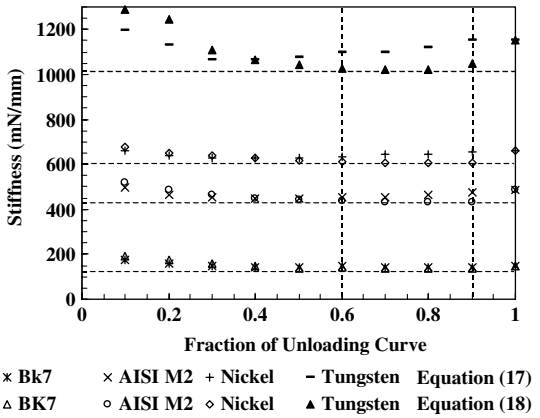

Fig. 7. Stiffness evolution with the fraction of the unloading curve considered in the fit of the points of the unloading curve, using Eqs. (16) and (17).

Table 5
Young's modulus results obtained in experimental and numerical tests using Eqs. (16) and (17) in the fits of unload curve for the stiffness evaluation

Results	BK7		Nickel		Steel AISI M2		Tungsten	
	Eq. (16)	Eq. (17)	Eq. (16)	Eq. (17)	Eq. (16)	Eq. (17)	Eq. (16)	Eq. (17)
Numerical								
P_{max} (mN)	10		10		20		20	
E_{Input}	82		220		220		410	
E (GPa)	91.5	86.5	261.0	239.3	243.9	229.1	511.4	451.7
Error (%)	11.6	5.5	18.3	8.5	10.9	3.9	24.7	10.2
r	0.9999	0.9999	0.9996	0.9999	0.9991	0.9999	0.9988	0.9999
Experimental								
P_{max} (mN)	42		42		100		42	
$E_{Reference}$	82		220		220		410	
E (GPa)	90.1	81.0	251.3	243.5	298.2	208.0	541.8	515.3
Error (%)	10.0	−1.1	14.2	10.7	35.2	−5.7	32.1	25.7
r	0.9997	0.9998	0.9998	0.9999	0.9999	0.9999	0.9996	0.9998

coefficients obtained in the fits are slightly better for the case of Eq. (17) than for Eq. (16). In order to check the efficacy of this analysis for experimental cases, ultramicrohardness tests were performed on the materials of Table 3. The comparative results using Eqs. (16) and (17) are also presented in Table 5, showing the improved performance of Eq. (16) also for experimental tests. In both cases, numerical and experimental, the fit used 70% of the unloading curve. As it was explained above, the numerical contact area used in the calculations corresponds to the interior of the contour defined by the nodes that contact with the indenter, at the maximum load; the experimental contact area was determined from contact indentation depth corrected with the indenter shape function.

This allows us to conclude that the stiffness evaluation, using a power law fit such as Eq. (17), enables us to obtain results with good accuracy, considering the upper unloading points in the above-mentioned range.

5.3. Indentation geometry

This section presents a study of the work hardening influence on the indentation geometry and consequently on the evaluation of the contact area. Numerical simulations with the indenter Vickers 3 (see Table 1), using the finite element mesh 2 previously presented (Table 2), were performed up to the same depth, $h_{max} = 0.3$ μm. A friction coefficient equal to 0.16 was assumed between the indenter and the sample. The fictitious materials simulated had two different Young' modulus (100 GPa and 410 GPa) and a Poisson's ratio of 0.29 (Table 4). The Swift Law (Eq. (8)) was used to model the material behaviour. Two different cases of work hardening coefficient, n, were studied: $n \approx 0$ (elastic-perfectly plastic materials) and $n = 0.6$ (high work-hardening materials). The yield stress values of the materials investigated are shown in Table 4.

Fig. 8 shows the indentation profiles obtained in the sample surface under indentation for each different work hardening materials and Young's modulus. In the figures, the indentation profiles appear related to the ratio h_f/h_{max}, between the indentation depth after unloading, h_f, and the indentation depth at the maximum load, h_{max}. The use of the ratio h_f/h_{max} as the analysis parameter is related to their simple determination based on the load–unload curves obtained in the numerical simulations or in the experimental tests. Furthermore, the parameter h_f/h_{max} apparently does not depend on the indentation depth, for a given material (Bolshakov et al., 1997).

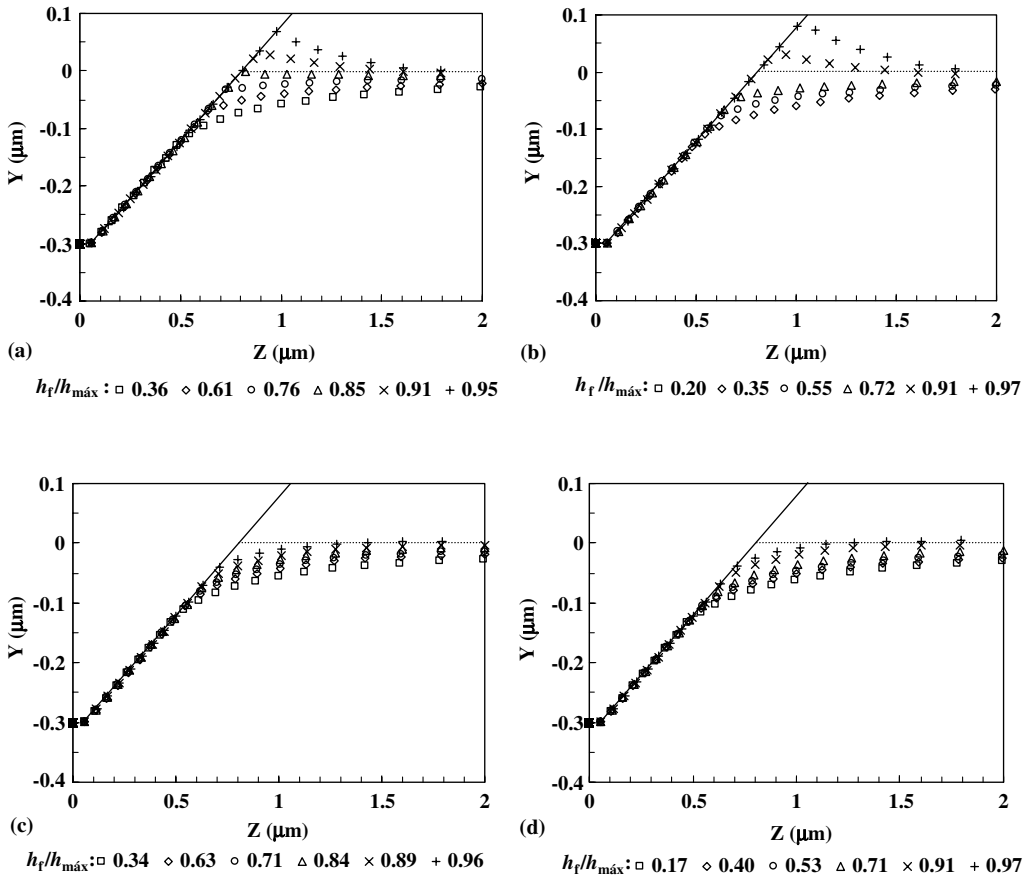

Fig. 8. Surface indentation profiles for different relations of h_f/h_{max}, with: (a) materials without work-hardening ($n \approx 0$) and $E = 100$ GPa; (b) materials without work-hardening ($n \approx 0$) and $E = 410$ GPa; (c) work-hardening materials ($n = 0.6$) and $E = 100$ GPa; (d) work-hardening materials ($n = 0.6$) and $E = 410$ GPa.

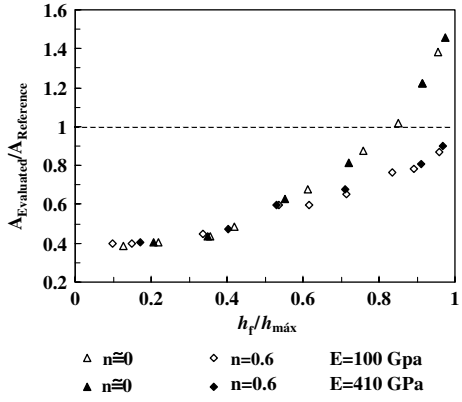

Fig. 9. Contact areas obtained from the finite element simulations.

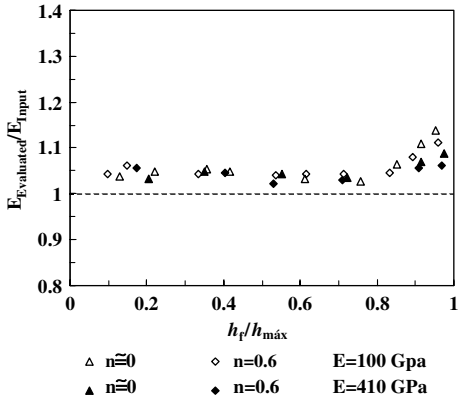

Fig. 10. Young's modulus results.

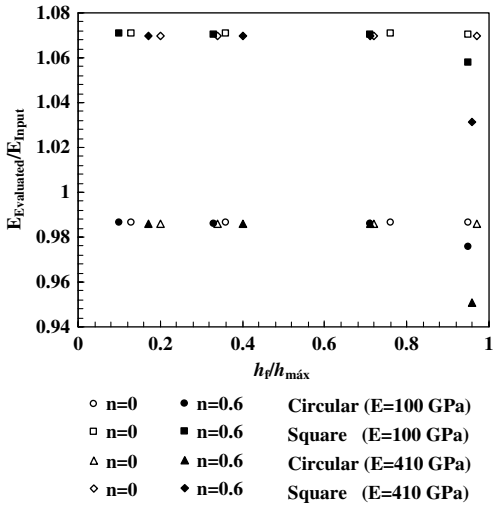

Fig. 11. Young's modulus results obtained for all the virtual materials with flat punches (circular and square geometries) and different contact areas.

Table 6
Calculated Young's modulus obtained for the tested flat indenters

Material	Indenter	Estimated E (GPa)	Input E (GPa)	Differences
AISI M2 steel	Circular	217	220	~−1.4%
	Square	236		~7.0%
BK7	Circular	81	82	~−0.9%
	Square	85		~3.8%
Tungsten	Circular	404	410	~−1.3%
	Square	439		~7.1%
Nickel	Circular	216	220	~−2.2%
	Square	237		~7.8%

Fig. 8(a) and (b) show that the pile-up formation appear associated to low values of work hardening ($n \approx 0$) and ratios $h_f/h_{max} > 0.8$. On the other hand, for materials with high work hardening coefficient ($n = 0.6$, in Fig. 8(c) and (d)), pile-up does not occur, whatever the value of h_f/h_{max} for any value of the indentation depth ratio h_f/h_{max}. Qualitatively similar results were obtained by other authors (Bolshakov et al., 1997), for a cone without friction between the sample and the indenter in 2D finite elements simulation.

Fig. 9 presents the projected contact area, $A_{Evaluated}$, obtained in the numerical simulations as a function of the ratio h_f/h_{max}. The contact area is normalized with respect to the projected reference area $A_{reference}$ (the area function of the indenter was taken into consideration) obtained when the indentation geometry does not present pile-up or sink-in formation. When the ratio $h_f/h_{max} < 0.6$, the contact area almost does not

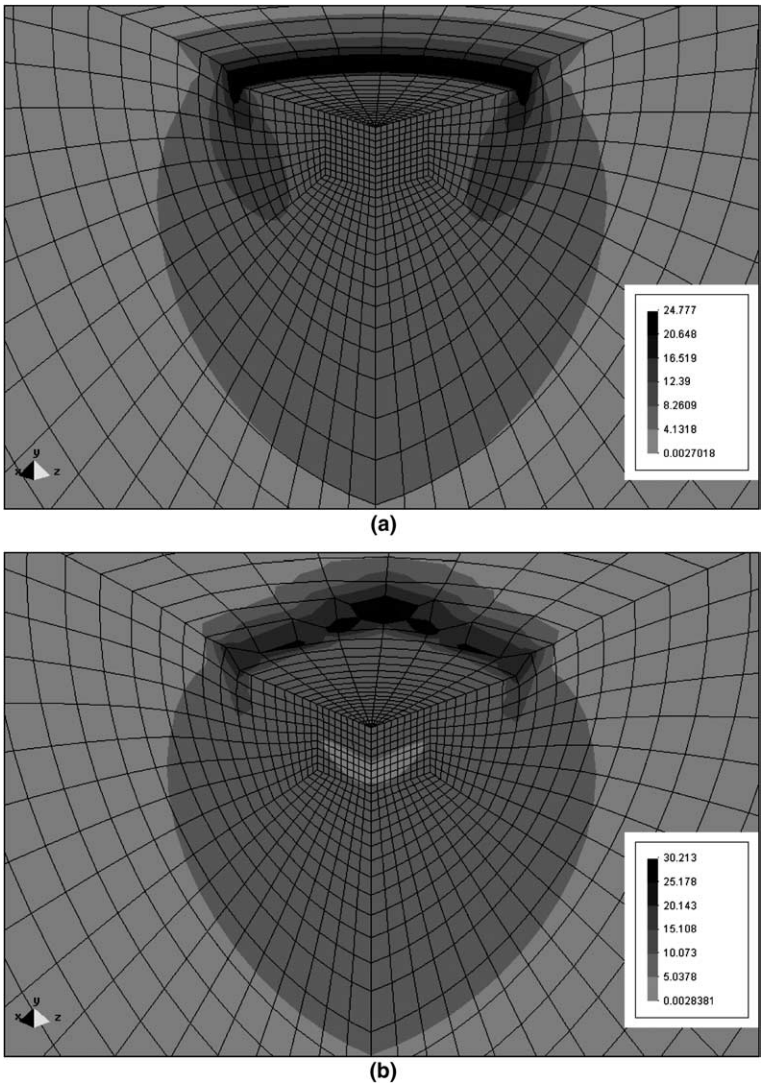

Fig. 12. Equivalent stress distribution at maximum load obtained in the steel AISI M2: (a) circular flat punch, with a contact area equal to 7 μm^2; (b) square flat punch, with a contact area equal to 7 μm^2.

depend on the work hardening coefficient and on the value of the Young's modulus. The ratio $A_{\text{Evaluated}}/A_{\text{reference}}$ is always less than 1, except for the values of $h_f/h_{max} > 0.85$, when $n = 0$. For $h_f/h_{max} > 0.6$, the normalized projected contact area depends on the work-hardening coefficient.

With the previous estimations for the contact area, an evaluation of the Young's modulus, E, was performed. These results are shown in Fig. 10, where the Young's modulus values, E, are normalized with respect to the input value, E_{input}, considered in the finite element simulations. From this figure, it is possible to see that $E_{\text{Evaluated}}/E_{\text{input}}$ is always higher than 1, being approximately close to 1.05, except for $h_f/h_{max} > 0.9$. In this region, the values of the ratio $E_{\text{Evaluated}}/E_{\text{input}}$ can attain values higher than 1.10. Identical results were obtained with conical indenters (Oliver and Pharr, 2004).

The overestimation in the evaluation of Young's modulus observed, whatever the value of h_f/h_{max}, can be related to the fact that the Vickers indenter geometry associated with large plastic deformations can not be perfectly described by Eq. (2). In order to remove this difficulty, a factor β is introduced in Eq. (2) so to take into account the fact that indentation experiments are performed with non-axisymmetric indenters and involving large plastic deformations. This way, Eq. (2) is usually written as follows:

$$E_R = \frac{1}{\beta}\frac{\sqrt{\pi}}{2}\frac{1}{\sqrt{A}}\frac{1}{C}. \tag{18}$$

In a recent review Oliver and Pharr (2004) state different values for the former proposed factor β, which they summarize as being in the range $1.0226 \leqslant \beta \leqslant 1.085$, for the Berkovich indenter. Most of the previous results concern circular geometries of the indenters, such as conical and flat-ended punches, 2D numerical

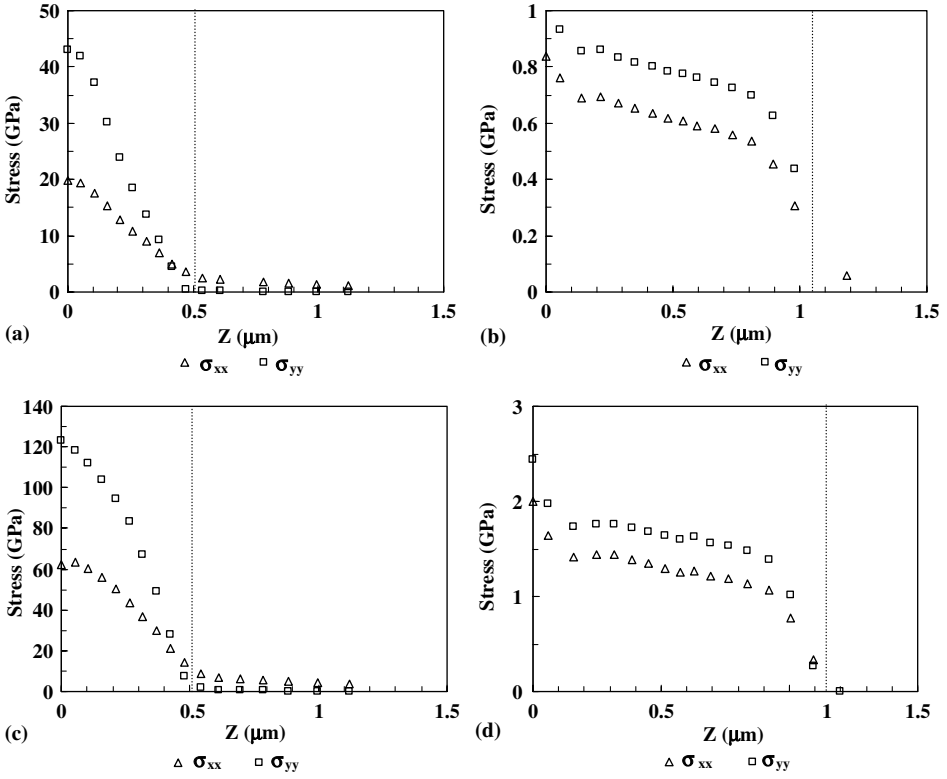

Fig. 13. Stress distributions obtained in the material with and $n \approx 0$: (a) $E = 100$ GPa and $h_f/h_{max} = 0.05$; (b) $E = 100$ GPa and $h_f/h_{max} = 0.95$; (c) $E = 410$ GPa and $h_f/h_{max} = 0.2$; (d) $E = 410$ GPa and $h_f/h_{max} = 0.97$.

simulations without friction (Oliver and Pharr, 2004; Bolshakov and Pharr, 1998; Hay et al., 1999; Cheng and Cheng, 1998, 1999). The present results overcome such difficulties and concern a large range of mechanical properties of the materials. The results in Fig. 10 indicate a mean value for the β factor close to 1.05, excepted for materials for which $h_f/h_{max} > 0.9$ for which β can be greater than 1.10. It must be remembered that the present results for β were obtained in 3D numerical simulation of Vickers Hardness tests of several materials with different Young's modulus and work hardening coefficients, and considering friction between the specimen and the indenter.

In order to better understand the role of the β factor and in which way its value is affected by the more or less severe plastic deformation that alter the surface orientation during the hardness indentation, we used the same materials that in Fig. 10 for tests with flat-ended punches, having circular and square shapes with three different area values (≈7, 21 and 41 μm^2). Simulations were performed with flat punches, using a 0.04 μm displacement imposed, in such away that only elastic deformation occurs. A friction coefficient equal to 0.16 was used in all the numerical simulations. The finite element mesh used was the mesh 2 (Table 2). The resulting Young's modulus values E are shown in Fig. 11 for each shape. This study was also performed in real materials and the conclusions are similar (Table 6). The value of E is always higher in the case of the square punch. This is certainly related with the stress and strain distribution under the indenter. Fig. 12(a) and (b) show the equivalent stress distribution at maximum load for both geometries, circular and square, and smaller areas for the case of the AISI steel. In the case of square geometry (Fig. 12(b)), the highest

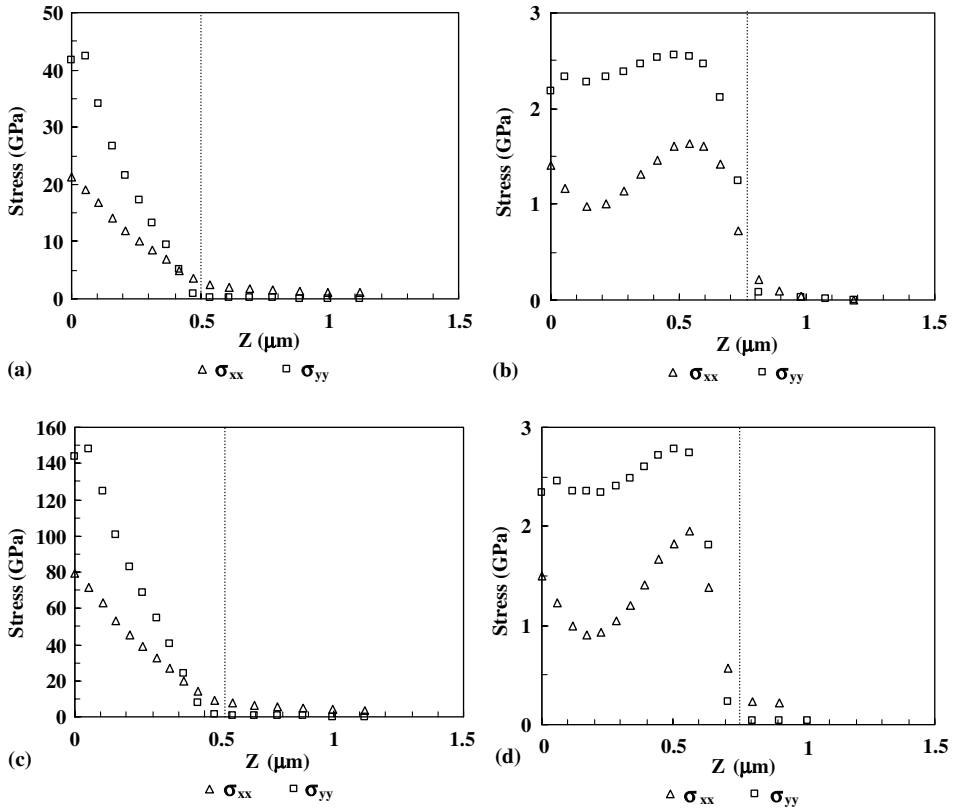

Fig. 14. Stress distributions obtained in the material with and $n = 0.6$: (a) $E = 100$ GPa and $h_f/h_{max} = 0.1$; (b) $E = 100$ GPa and $h_f/h_{max} = 0.89$; (c) $E = 410$ GPa and $h_f/h_{max} = 0.17$; (d) $E = 410$ GPa and $h_f/h_{max} = 0.97$.

stresses are observed near the corners. Considering that Equation (2) results from the Sneddon's analysis (Sneddon, 1965), for purely elastic contact of a rigid cone, the present results indicate that its use for the case of a square flat punches needs a correction, by using the β parameter. This study with flat indenters shows the simple consideration of a square geometry (β mean value equal to 1.085) instead of a circular one: (β mean value equal to 0.99) which is quite close to 1.

Results by Giannakopoulos et al. (1994) and Larsson et al. (1996), with 3D numerical simulations shows that for the Berkovich and Vickers indenters the value of β depends on the Poisson's ratio v and its values for $v = 0.3$ are $\beta = 1.14$ and 1.095, respectively. Moreover, most of the results presented in the literature show that the β value is higher for the Berkovich than for the Vickers indenter, increasing with the apical half-angle, which are in agreement with our β values (1.05 for the real Vickers indenter and 1.085 for the

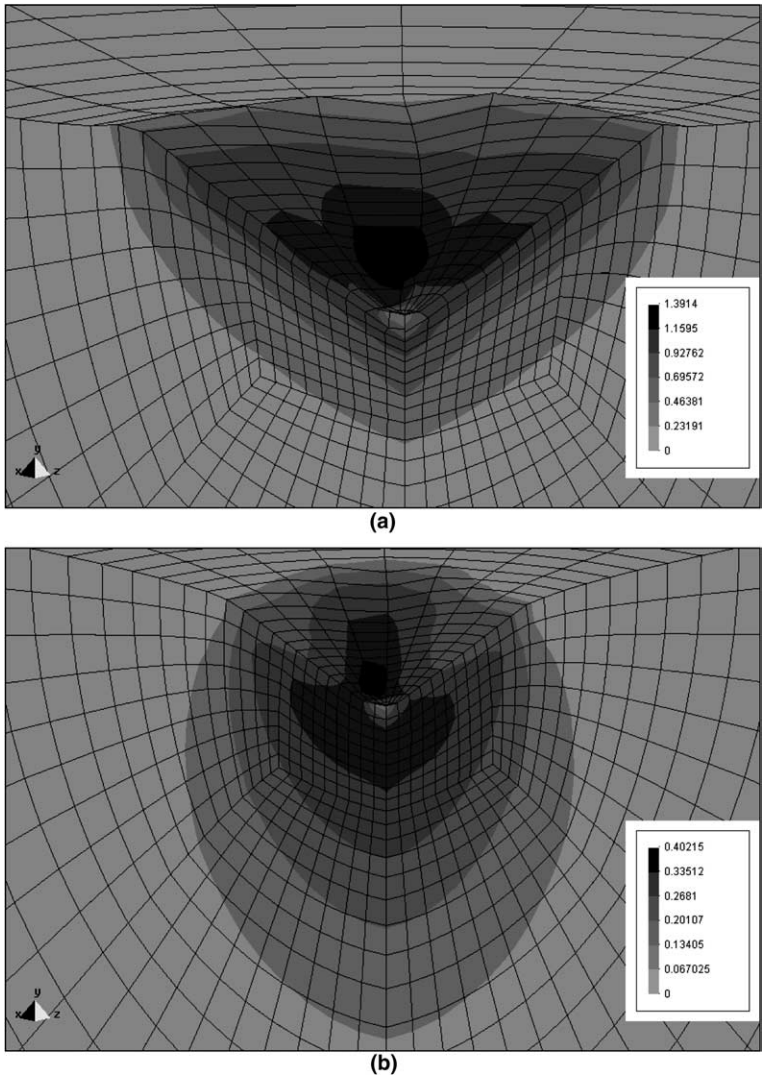

Fig. 15. Equivalent plastic strain distribution at maximum load for the materials with $E = 100$ GPa: (a) yield stress equal to 0.25 GPa and $n \approx 0$; (b) yield stress equal to 0.05 GPa and $n = 0.6$.

square flat punch). The difference between β values for square flat punch and for the Vickers indenter can be related with the fact that in the flat ended punch only the material elastic deformation occurs. On the other hand, for the Vickers indenter, severe plastic deformation appears which distorts the surface during the hardness indentation.

5.4. Stress and strain distributions

Stress distributions of σ_{xx} and σ_{yy} (see Fig. 1) obtained with the tested materials, are presented in Figs. 13 and 14. For the different cases studied (four combinations of: $E = 100$ and 410 GPa; $n \approx 0$ and $n = 0.6$), only the minimum and the maximum values of h_f/h_{max} tested in each case are presented. The results

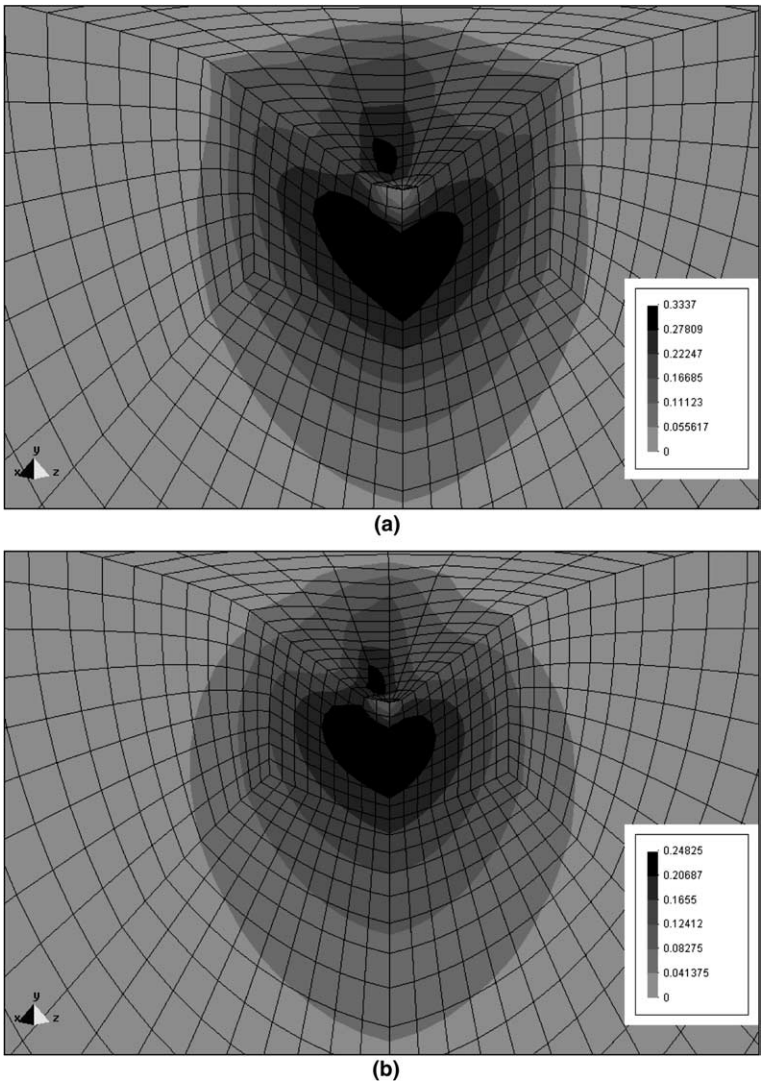

Fig. 16. Equivalent plastic strain distribution at maximum load for the materials with $E = 100$ GPa: (a) yield stress equal to 4 GPa and $n \approx 0$; (b) yield stress equal to 0.75 GPa and $n = 0.6$.

presented in the figures correspond to the absolute values of the compressive stresses, which were obtained at the surface of the indentation, at the same indentation depth.

The stress distributions presented in the figures show that the zones with compressive stresses correspond to the total length in contact with the indenter (the vertical dashed line in figures represents the contact boundary). For high values of the ratio h_f/h_{max}, which correspond to materials with relatively low yield stresses, the obtained stress level is low and rather horizontal as shown in Fig. 13(b) and (d) and Fig. 14(b) and (d). For the cases of Fig. 13(b) and (d) ($n = 0$), pile-up appears in the indentation, which is not the case of Fig. 14(b) and (d) ($n = 0.6$). For low values of the ratio h_f/h_{max}, which correspond to materials with relatively high yield stresses (sink-in occurs for $n = 0$ and for $n = 0.6$), the stress distributions obtained are triangular and quite similar for all cases (Fig. 13(a) and (c) and Fig. 14(a) and (c)).

Fig. 15(a) and (b) show the equivalent plastic deformation obtained with h_f/h_{max} values close to one for the two work hardening considered in the materials with $E = 100$ GPa ($h_f/h_{max} = 0.95$ and 0.96 for $n \approx 0$ and 0.6, respectively). From Fig. 15(a), it is possible to see pile-up formation where there is low work hardening (and low yield stresses $h_f/h_{max} = 0.95$). Among all studied cases, this one presents the highest value of equivalent plastic deformation. It must be mentioned that the figures present a difference between maximum values of the plastic deformation around 71%. Moreover, the plastic strain region is deeper than larger, when $n = 0.6$, being larger than deeper for $n \approx 0$. In Fig. 16(a) and (b) are shown the cases of ratios h_f/h_{max} equal to 0.6 and materials with highest yield stresses (among all studied cases) and $E = 100$ GPa

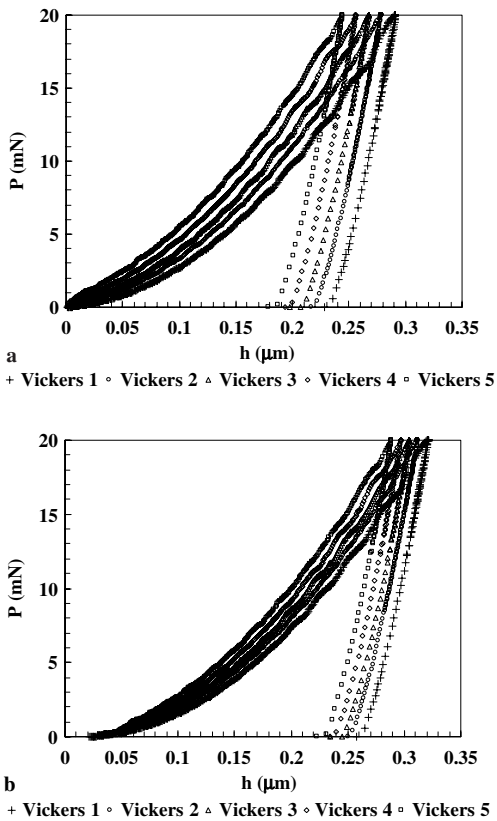

Fig. 17. Numerical load–unload curves obtained for the case of M2 Steel: (a) without offset correction; (b) with offset correction.

($h_f/h_{max} = 0.61$ for $n \approx 0$ and $h_f/h_{max} = 0.63$ for $n = 0.6$), the maximum values of equivalent plastic strain becomes lower, as well as the difference between both cases (≈25%). Qualitatively similar results were obtain for the case of the materials with $E = 410$ GPa. Being so, we conclude that for a given value of the ratio h_f/h_{max}, the maximum value of plastic deformation involved in the indentation process increases with the decreasing of the work hardening. This suggests that a high value of the work-hardening coefficient distribute the deformation under the indentation in a more homogeneous way than a low value of the work-hardening coefficient. Furthermore, for the low work hardening value ($n = 0$), the maximum values of the plastic deformation appear at the surface in contact with the indenter, which can lead to the pile-up formation through the material dislocation along the surface of the indentation.

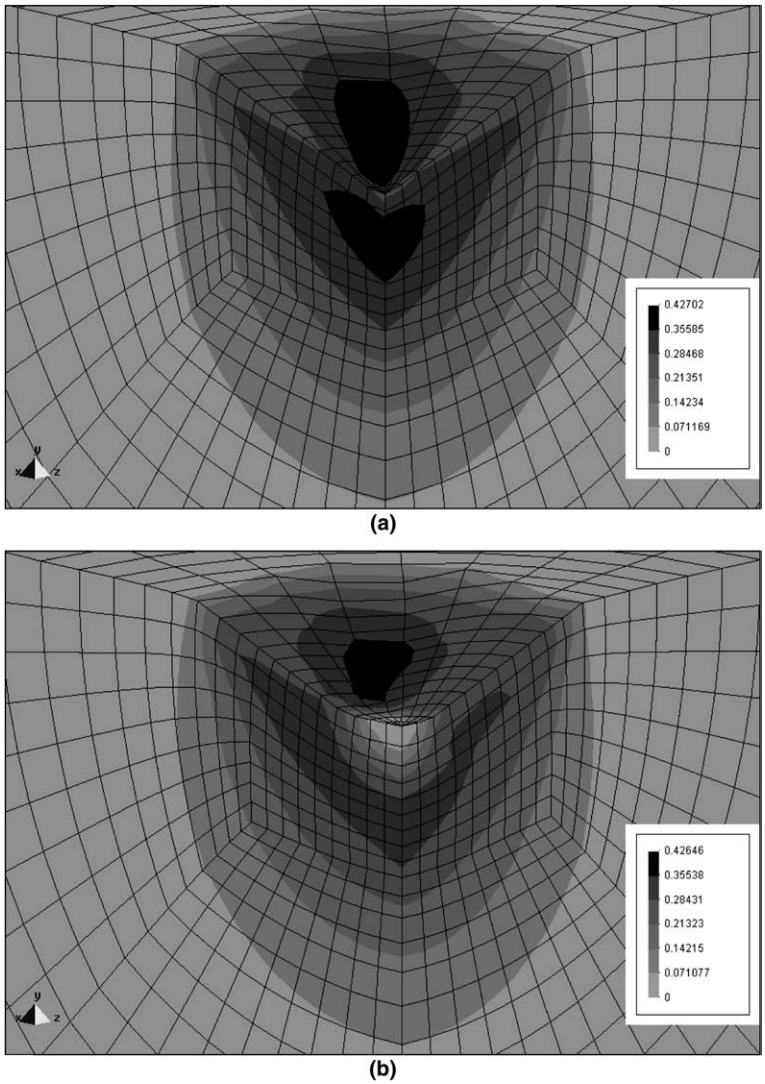

Fig. 18. Equivalent plastic strain distribution at maximum load obtained for the AISI M2 steel: (a) Indenter Vickers 1; (b) Indenter Vickers 5.

5.5. Indenter tip imperfections

Numerical simulations were performed using the five offsets and the four real materials above mentioned (see Tables 1 and 3, respectively). This allows us to study the influence of the size of the Vickers offset on the mechanical properties evaluation. The maximum loads applied were chosen in such a way that the indentation depths are approximately equal, for all the considered materials (≈0.25 μm, for Vickers 3).

Fig. 17(a) shows the curves load (P) versus the depth (h) for the five cases of Vickers indenters up to $P_{max} = 20$ mN, for the case of M2 steel. The maximum value of the indentation depth (h_f/h_{max}) increases as the size of the indenter offset decreases. The same curves, with the offset correction are presented in Fig. 17(b). The correction was carried out by taking into consideration the function area of each indenter. The curves become closer to each other, but not coincident. This behaviour was observed for the other three tested materials (Table 3). Fig. 18(a) and (b) present the equivalent strain distribution, at maximum load, for the tests with Vickers 1 and 5, respectively. From these figures, it can be concluded that the maximum values of the equivalent strain (≈0.42) are about the same for both cases. Also under the centre of the offset region, the deformation is almost zero, for Vickers 5. This fact can be justified by the presence of a hydrostatic stress state, in this region, which increases with the increasing of the value of the offset. In a region below the indentation, a higher plastic deformation appears, for the cases of low values of offset (Fig. 18(a)).

For the five indenters offsets tested, the Young's modulus of the four studied real materials was evaluated from the load–unload curves, following the considerations described above, and using Eqs. (2) and (3). In Eq. (2) the term C, represents the compliance at the beginning of the unloading curve; these values were determined by fitting 70% of the unloading curve with Eq. (18). The Young's modulus results obtained for the four tested materials are shown in Fig. 19.

The values of Young's modulus obtained for the AISI M2 steel and BK7 are always 5.5% and 3.9% higher than the one used as the input data ($E = 220$ and 82 GPa) of the simulations (Table 3). In the case of the nickel and tungsten, the values are 5.5% and 10.2% higher than the input Young's modulus values equal to 220 and 410 GPa, respectively. These results of Young's modulus were obtained with the indenter Vickers 3 (Table 1). These deviations are in agreement with the ones obtained for the virtual materials with the same h_f/h_{max} and indenter offset values (Fig. 10).

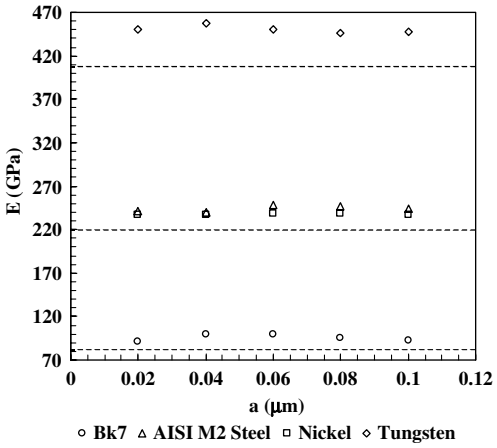

Fig. 19. Young's modulus results obtained with the five tested Vickers indenters.

Table 7
Values of evaluated hardness (GPa)

Indenter	Steel AISI M2		BK7		Tungsten		Nickel	
	E (GPa)	H (GPa)	E (GPa)	H (GPa)	E (GPa)	H (GPa)	E (GPa)	H (GPa)
Vickers 1	230.2	9.5	85.9	6.7	447.5	5.8	236.8	2.4
Vickers 2	230.5	9.6	86.4	7.3	445.5	5.7	238.7	2.4
Vickers 3	229.1	9.9	86.5	7.1	449.9	5.8	238.3	2.4
Vickers 4	225.2	10.1	87.4	7.1	456.9	5.8	237.4	2.5
Vickers 5	224.5	10.1	83.5	6.9	449.9	5.8	237.5	2.5
Differences	2.7%	5.9%	4.5%	8.2%	2.5%	1.7%	0.8%	4%

Young's modulus and hardness values evaluated for the four materials with the five Vickers indenters are presented in Table 7. The differences obtained for Young's modulus and hardness values with the five indenters, can suggest an apparent independence from the Vickers offset dimension.

6. Conclusion

Results of finite element simulations of ultramicrohardness tests presented highlight the ability of finite element code HAFILM to simulate this type of tests. The analysis of the refinement of the finite element mesh presented, show the importance of this parameter on the evaluation of the mechanical properties. The results of the finite element simulations enable us to state that a friction coefficient equal to 0.16 can be used to describe the contact with friction between the indenter and the sample material. The compliance results obtained with the method proposed, allows us to conclude that the consideration of 60% to 90% of the unload curve enable to obtain good accuracy.

The special care taken in the Vickers indenter modulation, enable us to better understand the influence of geometric imperfections, such as, the offset on the evaluation of the mechanical properties. Moreover, results from numerical simulations flat punch of different geometry and size show the influence of the geometry on the refereed properties. Finally, the study of the indentation geometry presented has shown the importance of its consideration in the contact area evaluation and consequently in the mechanical properties results. It also shown that the parameter h_f/h_{max}, can be used as an indicator when pile-up or sink-in may be an important factor, that can be easily determined from the experimental curves.

Acknowledgements

The authors acknowledge Fundação para a Ciência e Tecnologia do Ministério da Ciência e Tecnologia for the financial support. The mechanical properties of the steel AISI M2, bK7 and nickel were kindly provided by the EC under contract STM4-CT98-2249 INDICOAT.

References

Alves, J.L., Menezes, L.F., 2002. Resolução de sistemas lineares esparsos em simulação 3-D do processo de conformação de chapa. Estudo da influência da numeração da malha, pré-condicionador e do método iterativo. In: V Congresso Métodos Numéricos En Ingeneria, Madrid, Spain.

Antunes, J.M., Cavaleiro, A., Menezes, L.F., Simões, M.I., Fernandes, J.V., 2002a. Ultra-microhardness testing procedure with Vickers indenter. Surface and Coatings Technology 149 (1), 27–35.

Antunes, J.M., Menezes, L.F., Fernandes, J.V., 2002b. Numerical study of the influence of imperfection of the tip of a Vickers indenter on ultramicrohardness. Key Engineering Materials 230 (1–2), 525–528.

Bowden, F.P., Tabor, D., 1950. The Friction and Lubrication in Solids, vol. 11, Clarendon Press.

Bhattacharya, A.K., Nix, W.D., 1988. Finite element simulation of indentation experiments. International Journal of Solids and Structures 24, 881–891.

Bhattacharya, A.K., Nix, W.D., 1991. Finite-element analysis of cone indentation. International Journal of Solids and Structures 27 (8), 1047–1058.

Bolshakov, A., Oliver, W.C., Pharr, G.M., 1996. Influences of stress on the measurement of mechanical properties using nanoindentation. Journal of Materials Research 11 (3), 760–768.

Bolshakov, A., Oliver, W.C., Pharr, G.M., 1997. Materials Research Society. Symposium. Proceedings.

Bolshakov, A., Pharr, G.M., 1998. Influences of pileup on the measurement of mechanical properties by load and depth sensing indentation techniques. Journal of Materials Research 13 (4), 1049–1058.

Cai, X., Bangert, H., 1995. Hardness measurements of thin films-determining the critical ratio of depth to thickness using FEM. Thin Solid Films 264 (1), 59–71.

Cheng, Y.-T., Cheng, C.-M., 1998. Scaling approach to conical indentation in elastic–plastic solids with work hardening. Journal of Applied Physics 84 (3), 1284–1291.

Cheng, Y.-T., Cheng, C.-M., 1999. Scaling relationships in conical indentation of perfectly elastic–plastic solids. International Journal of Solids Structures 36 (8), 1231–1243.

Desaxce, G., Feng, Z.Q., 1991. New inequality and functional for contact with friction—the implicit standard material approach. Mechanics of Structures and Machines 19 (3), 301–325.

Doerner, M.F., Nix, W.D., 1986. A method for interpreting the data from depth-sensing indentation instruments. Journal of Materials Research 1 (9), 601–609.

Giannakopoulos, A.E., Larson, P.-L., Soderlund, E., Rowcliffe, D.J., Vestergaard, R., 1994. Analysis of Vickers indentation. International Journal of Solids and Structures 31 (19), 2679–2708.

Hay, J.C., Bolshakov, A., Pharr, G.M., 1999. A critical examination of the fundamental relations used in the analysis of nanoindentation data. Journal of Materials Research 14 (6), 2296–2305.

Kral, E.R., Komvopoulos, K., Bogy, D.B., 1993. Elastic–plastic finite-element analysis of repeated indentation of a half-space by rigid sphere. Journal Applied Mechanics 60 (4), 829–841.

Laursen, T.A., Simo, J.C., 1992. A study of the mechanics of microindentation using finite-elements. Journal of Materials Research 7 (3), 618–626.

Larsson, P.-L., Giannakopoulos, A.E., Vestergaard, R., 1996. Analysis of Berkovich indentation. International Journal of Solids Structures 33 (2), 221–248.

Lynch, C.T., 1980. Handbook of Materials Science, vol. 11, General Properties CRC Press.

Menezes, L.F., Teodosiu, C., 2000. Three-dimensional numerical simulation of the deep-drawing process using solid finite elements. Journal of Materials Processing Technology 97 (1–3), 100–106.

Murakami, Y., Yuang, L.P, 1992. Finite-element method (FEM) analysis of elastic-linear-hardening materials and comparison with measurements on commercial materials. Journal of Testing and Evaluation 20 (1), 15–24.

Oliveira, M.C., Alves, J.L., Menezes, L.F., 2003. Improvement of a frictional contact algorithm for a strongly curved contact problems. International Journal for Numerical Methods in Engineering 58, 2083–2101.

Oliver, W.C., Pharr, G.M., 1992. An improved technique for determining hardness and elastic- modulus using load and displacement sensing indentation experiments. Journal of Materials Research 7 (6), 1564–1583.

Oliver, W.C., Pharr, G.M., 2004. Measurement of hardness and elastic modulus by instrumented indentation: Advances in understanding and refinements to methodology. Journal of Materials Research 19 (1), 3–20.

Simo, J.C., Laursen, T.A., 1992. An Augmented Lagrangian treatment of contact problems involving friction. Computers and Structures 42 (1), 97–116.

Sneddon, I.N., 1965. The relation between load and penetration in the axisymmetric Boussinesq problem for a punch of arbitrary profile. International Journal of Engineering Science 3, 47–56.

Sun, Y., Bell, T., Zheng, S., 1995. Finite-element analysis of the critical ratio of coating thickness to indentation depth for coating property measurements by nanoindentation. Thin Solid Films 258 (1–2), 198–204.

Taljat, B., Zacharia, T., Kosel, F., 1998. New analytical procedure to determine stress-strain curve from spherical indentation data. International Journal of Solids Structures 35 (33), 4411–4426.

Trindade, A.C., Cavaleiro, A., Fernandes, J.V., 1994. Estimation of Young's modulus and hardness by ultra-low load hardness tests with a Vickers indenter. Journal of Testing and Evaluation 22 (4), 365–369.

Wang, H.F., Bangert, H., 1993. 3-Dimensional finite-element simulation of Vickers indentation on coated systems. Materials Science and Engineering A: Structural Materials and Processing 163 (1), 43–50.

Zeng, K., Giannakopoulos, Rowcliffe, D.J, 1995. Vickers indentations in glass. Comparison of finite-element analysis and experimentes. Acta Materialia 43 (5), 1945–1954.